

Analyst

Accepted Manuscript



This is an *Accepted Manuscript*, which has been through the Royal Society of Chemistry peer review process and has been accepted for publication.

Accepted Manuscripts are published online shortly after acceptance, before technical editing, formatting and proof reading. Using this free service, authors can make their results available to the community, in citable form, before we publish the edited article. We will replace this *Accepted Manuscript* with the edited and formatted *Advance Article* as soon as it is available.

You can find more information about *Accepted Manuscripts* in the [Information for Authors](#).

Please note that technical editing may introduce minor changes to the text and/or graphics, which may alter content. The journal's standard [Terms & Conditions](#) and the [Ethical guidelines](#) still apply. In no event shall the Royal Society of Chemistry be held responsible for any errors or omissions in this *Accepted Manuscript* or any consequences arising from the use of any information it contains.

Rapid identification of goblet cells in unstained colon thin sections by means of quantum cascade laser-based infrared microspectroscopy†

Cite this: DOI: 10.1039/x0xx00000x

Received 00th January 2012,
Accepted 00th January 2012

DOI: 10.1039/x0xx00000x

www.rsc.org/

N. Kröger-Lui,^{*a} N. Gretz,^b K. Haase,^a B. Kränzlin,^b S. Neudecker,^b A. Pucci,^a A. Regenscheit,^a A. Schönhals^a and W. Petrich^a ‡

Changes in the volume covered by mucin-secreting goblet cell regions within colon thin sections may serve as a mean to differentiate between ulcerative colitis and infectious colitis. Here we show that the rapid, quantum cascade laser-based mid-infrared microspectroscopy might be able to contribute to the differential diagnosis of colitis ulcerosa, an inflammatory bowel disease. Infrared hyperspectral images of mouse colon thin sections are obtained within 7.5 minutes per section with a pixel size of 3.65 x 3.65 μm^2 and a field of view of 2.8 x 3.1 mm^2 . The spectra are processed by training a random decision forest classifier on the basis of k-means clustering on one thin section. The trained algorithm was then applied to 5 further thin sections for a blinded validation and it was able to identify the goblet cells in all sections. The rapid identification of goblet cells within these unstained, paraffinized thin sections of colon tissue is enabled by the high content of glycopeptides within the goblet cells as revealed by the pronounced spectral signatures in the 7.6 μm – 8.6 μm and the 9.2 μm – 9.7 μm wavelength ranges of the electromagnetic spectrum. Even more so, the simple calculation of the ratio between the absorbance values at 9.29 μm and 8.47 μm provides the potential to further shorten the time for measurement and analysis of a thin section down to well below 1 minute.

Introduction

Among the autoimmune disorders of the digestive system is the inflammatory bowel disease (IBD). Ulcerative colitis and Crohn's disease constitute the most prevalent forms of idiopathic IBD. These chronic inflammatory disorders of the gastrointestinal tract are characterized by distinct modifications of clinical, pathological, endoscopic and radiological features.^{1,2}

In practice, a common problem is the differentiation of an infectious colitis from an inflammatory bowel disease such as ulcerative colitis. While some severe cases of infectious colitis need to be treated with antibiotics, ulcerative colitis is usually treated in a different manner. Diagnosis of ulcerative colitis and the differentiation from other conditions is done by the interpretation of biopsies in combination with clinical, laboratory, radiographic and endoscopic observations. One of the histological characteristics to distinguish between these two vastly different forms of colitis might be achieved by comparing the amount of epithelial goblet cells in colonic mucosa: While ulcerative colitis will cause a depletion (or emptying) of goblet cells³, non-chronic intestinal infections usually do not affect the size of the histological area containing

goblet cells. Further examples for changes in goblet cell population caused by intestinal infections include hyperplasia caused by helminth infections and the depletion in population caused by chronic infections.⁴⁻⁶

In those cases, in which gastrointestinal biopsies are performed, standard histopathology is performed on stained thin sections that originate from the biopsies. For general purposes, including the highlighting of goblet cells, haematoxylin and eosin (H&E) staining is used. As goblet cells produce mucins, Alcian blue and PAS staining can be used to highlight the goblet cell population.

Due to recent technical advances, the reagent-free assessment of tissue thin sections raises increased interest. The use of light sources of high spectral power density in the mid-infrared spectral region, namely tunable quantum cascade lasers (QCLs)⁷, in combination with, potentially, low cost microbolometer arrays enables a rapid, reagent free analysis on the basis of mid-infrared microspectroscopy.⁸⁻¹¹ Beyond the initial reagent-free, QCL-based investigations of biomedical samples at a single wavelength *in vitro*^{9,12} and *in vivo*¹³, Kröger et al. were recently able to show in a one-to-one comparison, that the reagent-free chemical analysis of unstained tissue

1 samples can be performed within 5 minutes (as compared to
2 hours and days when using standard broadband FT-IR
3 microspectroscopy) using a tunable QCL.¹¹ While the
4 traditional FT-IR techniques offer a good signal-to-noise ratio
5 and a broad spectral range, extensive acquisition times are
6 needed for FT-IR microspectroscopy, which can only be
7 circumvented by costly equipment such as large, liquid nitrogen
8 cooled MCT array detectors or synchrotron radiation.

9 In this work we demonstrate the rapid visualization of
10 colonic mucosa via hyperspectral imaging using a QCL-based
11 setup with a particular emphasis on identification of goblet cell
12 rich regions in colonic epithelium.

13 **Materials and Methods**

14 **Colon samples**

15 A colon sample was obtained from a healthy male C57BL/6
16 mouse (age: 6 months). The sample was immersion fixed in 4%
17 buffered formaldehyde for 24h. and embedded in paraffin with
18 the help of an Leica TP1020. For this purpose, the sample was
19 post-fixed, dehydrated in a series of graded alcohol and
20 infiltrated with paraffin as follows: 4% buffered Formaldehyde
21 (2 x 1,5 h), 70% Ethanol (1,5 h), 80% Ethanol (1,5 h), 96%
22 Ethanol (1,5 h), 99% Ethanol (2 x 1,5 h), Xylol (2 x 1,5 h),
23 Paraffin (3 x 1,5 h). The tissue sample was collected according
24 to regulations of the German Animal Welfare Act (I13/10,
25 Animal Welfare Office, Medical Faculty Mannheim of the
26 University of Heidelberg). Two 8 μm thin sections were cut
27 using a Leica RM 2165 microtome. The thin sections were
28 placed on a barium fluoride substrate (Korth Kristalle GmbH,
29 Germany). Each slice features three colon tissue sections. For
30 comparison, multiple adjacent slices of 3 μm thickness were
31 prepared from the vicinity of the 8 μm thick section and
32 positioned on glass substrates for imaging with a standard
33 microscope (Zeiss Axio Scope.A1, Carl Zeiss Microscopy
34 GmbH, Germany). Haematoxylin and eosin (H&E) staining
35 was performed on the third adjacent slice per layer while Alcian
36 blue and PAS staining was performed on the first adjacent slice
37 per layer to visualize goblet cells.

38 **Infrared microscopy**

39 QCL-based infrared chemical imaging was enabled by the
40 home built setup described in. Ref. 10. Due to the particular
41 interest in goblet cells, the available spectral region needed to
42 include glycosylation bands which are typical markers for
43 mucins produced by goblet cells. For human colonic tissue,
44 glycosylation bands have been located at 1044, 1076 and 1125
45 cm^{-1} .¹⁴ According to literature, close similarities between the
46 spectral features of mouse and human colonic tissue can be
47 expected.¹⁵ Two quantum cascade lasers (Daylight Solutions
48 Inc., USA) were successively tuned through the wavenumber
49 regions between 1027-1087 cm^{-1} and 1167 1319 cm^{-1} ,
50 corresponding to wavelength ranges of 9.74 μm - 9.20 μm and
51 8.57 μm - 7.58 μm . For a sample measurement, each laser was
52 tuned over the entire tuning range within 11.3 seconds for 20

53 times. A 640 x 480 pixel microbolometer array (Infratec
54 GmbH, Germany) was used to record the transmission through
55 the sample at any given wavelength. The frame rate was 50 Hz.
56 All measurements were performed with a projected pixel pitch
57 in the sample plane of 3.65 μm . Two infrared lenses were used
58 for a 4:1 magnification. The field of view was amounted to
59 2.8x3.1 mm^2 . Spatial resolution was determined to be 9.4 \pm 1.8
60 μm (at 1065 cm^{-1}).

Synchronization of the laser tuning time and the bolometer
array's frame rate resulted in an effective wavenumber
resolution of 4 cm^{-1} which suffices for analyzing mid-infrared
spectra of paraffin-embedded tissue thin sections.^{16,17}

The total acquisition time for infrared microscope images
over the full lasers' tuning ranges was determined to be 7.5
minutes for each of the six samples. A single background
measurement was performed within additional 7.5 minutes once
in order to serve as a reference for all of the 6 hyperspectral
tissue images. Transmittance was calculated by normalizing the
single channel spectrum of the sample to that of the blank
substrate. Absorbance spectra were calculated as the negative
natural logarithm of the transmission spectra for each pixel
individually. No further pre-processing was performed apart
from the background correction, spectral binning (average bin
size 2.4 cm^{-1}), water vapour correction, and a Gaussian
smoothing filter with a size of 3 pixels. Spectral binning and
background correction can be performed at the measurement's
runtime. Water vapour correction was performed after
clustering and binning to adjust for the imperfect purging of the
microscope setup with dried air. As humidity did not match
perfectly between reference and sample measurements but was
constant during the sample measurements, water vapour
correction did not affect the clustering or classification results.

Because the lateral resolution is not limited by the pixel size
for the measurements described here, a small Gaussian filter
appears to be beneficial for the visual inspection of the images
since it reduces pixilation effects. While further data pre-
processing - especially scattering correction - would greatly
enhance the quality of the data, it is also very time consuming.
Depending on the application, the excessive amount of
computation time needed might not be justified.

43 **Data analysis**

When analyzing mid-infrared spectral image information, there
is the danger of so-called overfitting (see e.g. ref. 16). In order
to avoid overfitting we use a four-step approach:

- 1.) Random selection of one out of the six thin sections,
henceforth referred to as "training sample"
- 2.) Unsupervised classification of the sample data by using
the information from the training sample only. k-means
clustering was performed on the training dataset. A total
of 10 clusters were chosen, 3 of which were attributed to
paraffin spectra (dashed lines in Fig. 2 (d)) or blank
substrate and 7 were attributed to tissue (see, for
example, Ref. 18). A total of 323300 single spectra were

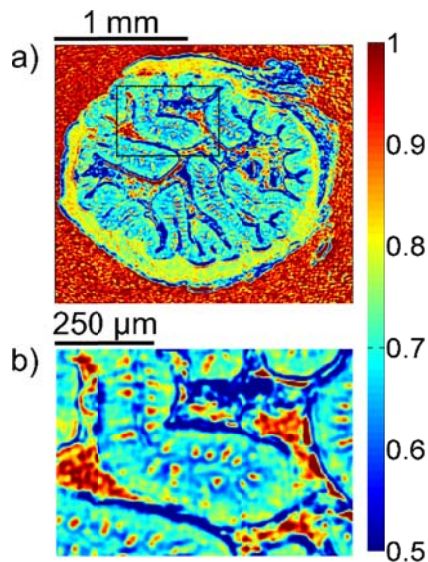
1 analysed. The resulting cluster memberships of these
2 spectra were used as ground truth for training of the
3 random decision forest classifier in step 3.

- 4 3.) Training of a random decision forest on the basis of step
5 2, whereby only the training sample is used. A total of
6 100 decision trees were grown (see, for example, Ref.
7 19).
8 4.) After steps 1-3, no retraining or changes of any kind are
9 acceptable. We then apply the trained random decision
10 forest to the remaining 5 thin sections ("blinded
11 validation") and provide an analysis of the outcome.
12 Each pixel was assigned to one of the 10 cluster groups
13 (which are resulting from k-means clustering) by
14 applying the random decision forest classifier.
15

16 All analyses were performed by means of MATLAB (R2014a,
17 TheMathWorks Inc., USA) on a standard computer with an
18 Intel® Core™ i7-3930k-CPU at 3.20 GHz and with 32 GB
19 RAM.
20

21 Results

22 A first impression of the quality of the image may be obtained
23 at a single wavelength already. In Fig. 1(a), infrared
24 transmission at 1218 cm^{-1} ($\pm 1.2\text{ cm}^{-1}$) through the entire colon
25 cross section is shown: The central lumen is surrounded by
26 colonic epithelium, connective tissue (lamina propria mucosae)
27 and smooth muscle tissue (lamina muscularis mucosae).
28 Surrounding the smooth muscle tissue, the paraffin matrix is
29 visible. A digital zoom (Fig. 1(b)) indicates a substructure in
30 the epithelium.
31
32



33
34
35
36
37
38
39
40
41
42
43
44
45
46
47
48
49
50
51
52 **Fig. 1** Infrared transmission of the colon sample. The data shown represents the
53 infrared transmission at 1218 cm^{-1} ($\pm 1.2\text{ cm}^{-1}$). (a) The complete tissue section,
54 including the surrounding smooth muscle tissue. (b) A digital zoom, highlighting
55 structures in the epithelium.

56 The single wavelength infrared image already reveals
57 surprisingly rich information about the tissue structure. For
58
59
60

further information, however, the full spectral ranges are
analyzed in the sense of step #2 of the analysis procedure,
namely k-means clustering ($k=10$). Figure 2 shows the results
of the k-means clustering of the slice used as a training set. In
the right column of Fig. 2.a-c the label image is shown. The 3
clusters with lowest average absorbance can be attributed to
paraffin of blank substrate and are coloured white for clarity.
Average spectra of each of the remaining 7 clusters are shown
in Fig. 2(d). In order to link the tissue clusters to tissue types,
the unstained slice (Fig. 2.a-c, central column) may be
compared to the cluster image and the H&E stained adjacent
slices (Fig. 2.a-c left column). Additionally, the distribution of
the green pixel class is compared to the microscopic image of
the Alcian blue and PAS stained colon tissue slice in Fig. 3.

In order to illustrate the predictive potential of the
classification scheme, a blinded validation was performed
(step#4 of section 2.3). The data originating from all tissue
sections of the validation set was visualized using the trained
random decision forest classifier. Results of the classification
can be seen in Fig.4. Analogous analysis of the remaining four
tissue sections can be found in the supplementary material
(Fig. S1–S4†).

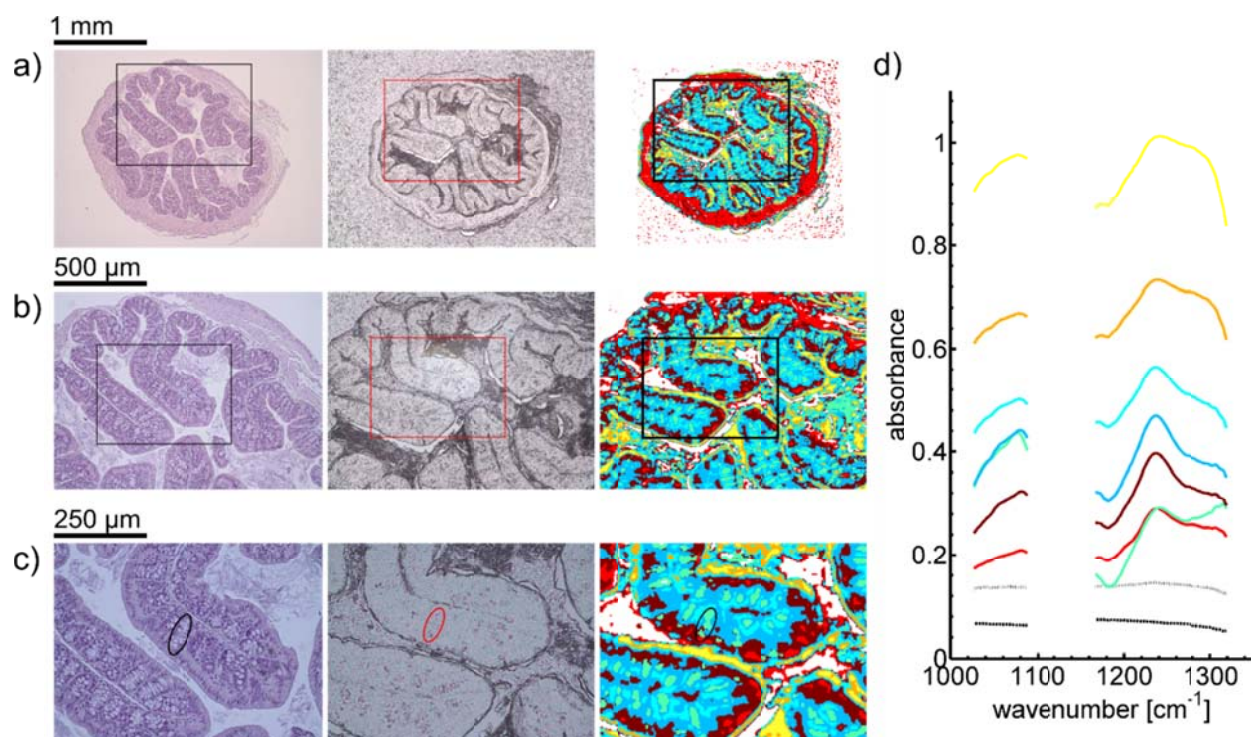


Fig. 2 (a)-(c) Microscopic image of a H&E stained colon slice (left column), an unstained colon tissue slice (central column), and label images obtained via k-means clustering of infrared data of the training set (right column). For the images of H&E stained and unstained slices, (a)-(c) represent optical zoom steps, with the magnified area highlighted by a box. The corresponding series of label images results from a digital zoom. Goblet cell rich regions in crypts are labelled green (marked by circle). (d) The mean cluster spectra obtained by clustering. Dashed lines represent the average spectra for clusters which were assigned to paraffin background.

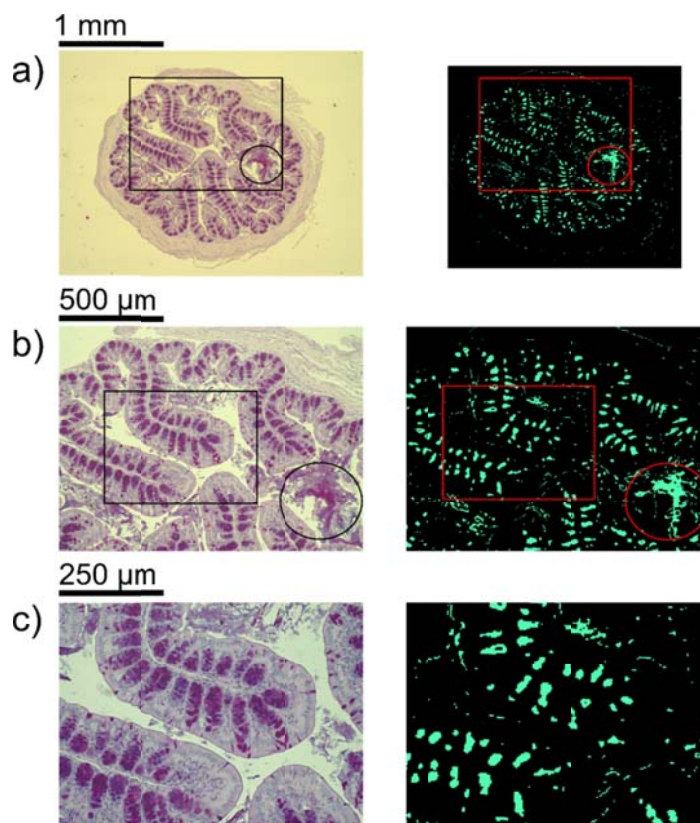


Fig. 3 (a)-(c) Microscopic image of Alcian blue and PAS stained colon slice (left column) and distribution of green pixels in label images obtained via k-means clustering of infrared data of the training set (right column). For the images of the Alcian blue and PAS stained slice, (a)-(c) represent optical zoom steps, with the magnified area highlighted by a box. The corresponding series of label images results from a digital zoom. An area with secreted mucus is highlighted by circles.

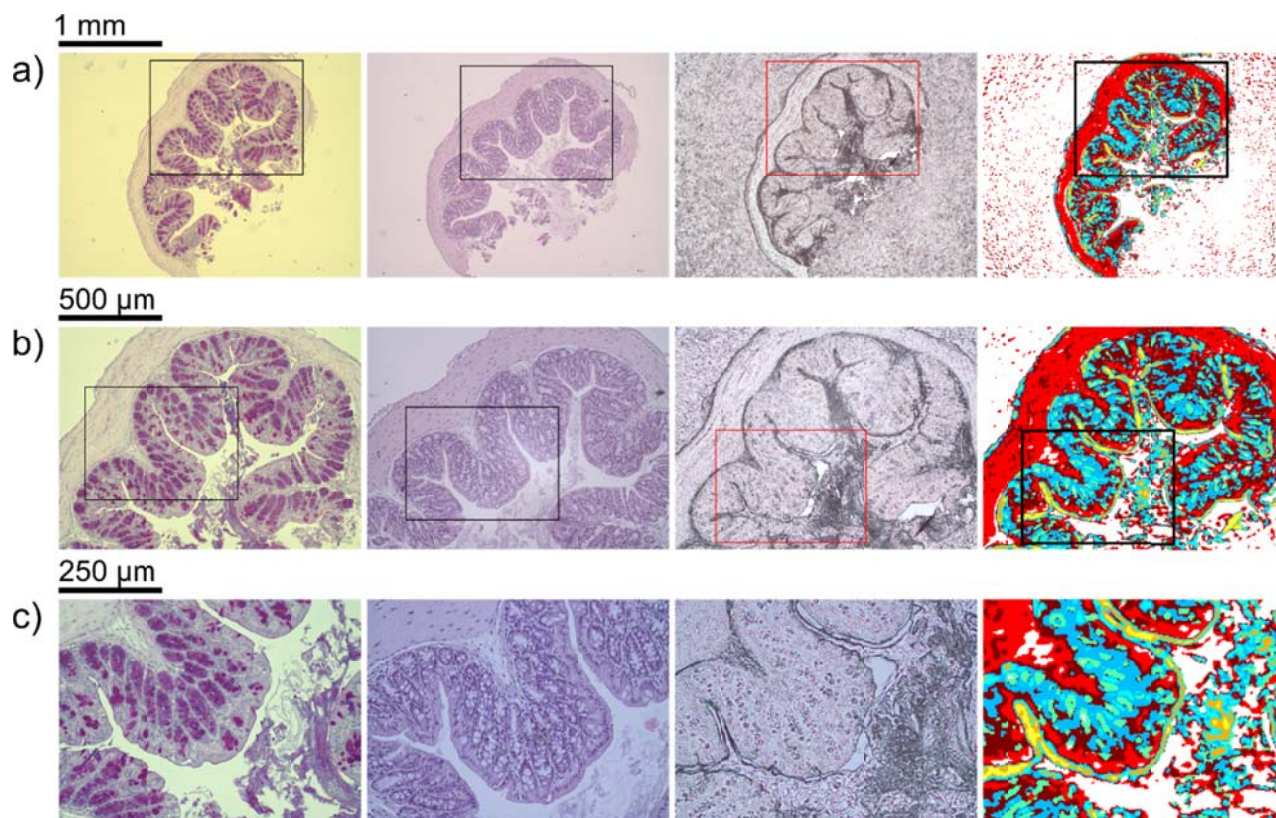


Fig. 4 (a)-(c) Microscopic image of an Alcian blue and PAS stained colon tissue slice, a H&E stained colon tissue slice, an unstained colon tissue slices, and label images obtained via random decision forest classification of infrared data (from left to right). For the images of H&E stained and unstained slices, the images (a)-(c) represent optical zoom steps, with the magnified area highlighted by a box. The corresponding series of label images results from a digital zoom.

Discussion

At first sight, the infrared images clearly resemble the morphology of the H&E stained as well as the unstained thin sections. However, given the spectral character of the acquired data, a further assignment of the features and their biochemical interpretation is desirable:

Globlet cell rich regions

Inside the colon, the mucin-containing mucus forms an essential barrier that protects the body from pathogens and irritants. Mucin is produced in the goblet cells that are present in colonic mucosa. Since mucin consists of highly glycosylated peptides, strong infrared absorption in the carbohydrate region ($1000\text{-}1100\text{ cm}^{-1}$) is expected. By comparing the result of the k-means clustering of the training set or the results of the random-decision forest classification of the validation set with Alcian blue and PAS stained colon tissue slices, the green pixel class appears to be strongly correlated to the location of patches with high goblet cell number. Note that an area containing secreted mucus in the central lumen (marked by circles in Fig.3) is also assigned to the green cluster, leading to the conclusion that areas of high mucin concentration are assigned to the green

class. This observation is supported by the increased ratio of absorbance in the carbohydrate spectral region, with a maximum absorbance at the glycosylation band at 1076 cm^{-1} , to the absorbance in the $1200\text{-}1300\text{ cm}^{-1}$ region. Analysis of the training data illustrates the potential for discrimination between different tissue types. The ratio of absorbances at 1076 cm^{-1} over 1181 cm^{-1} , for example, illustrates the potential for spectral differentiation between the mucin-producing goblet cells and the rest of the tissue (Table 1 and Fig. 5 (a)).

Muscularis (Lamina propria/ Enterocytes)

Surrounding each colon section, a ring representing the lamina muscularis is clearly visible. It is associated with the light red pixel class. This class features the lowest average absorbance of all classes not considered to be background spectra. Also, the lamina propria as well as some of the colon enterocytes are labelled with light red. The absorbance integral over the carbohydrate spectral region (see Table 1 and Fig. 5 (b)) may already suffice for a simplified differentiation between the *lamina muscularis* and the rest of the tissue.

Table 1 Overview of the color assignments. The ratio of absorbance at 1076 cm^{-1} over 1181 cm^{-1} and the absorbance integral from 1027 cm^{-1} to 1087 cm^{-1} was calculated for each pixel in the training set for the random decision forest classifier. For each pixel class defined by the initial k-means clustering, the median value of the results was calculated. The difference of median to the 5% and 95% quantile is given by $-\Delta q_{0.05}, +\Delta q_{0.95}$.

	Color	Biomedical association	Absorbance ratio: 1076 cm^{-1} /1181 cm^{-1} [arb. units]	Absorbance integral: 1027 cm^{-1} to 1087 cm^{-1} [arb. units]
Median $-\Delta q_{0.05}, +\Delta q_{0.95}$				
	Green	Mucin / goblet cells	2.97 -1.45,+7.24	26.07 -6.10,+5.95
	Light red	Lamina muscularis, Lamina propria, colon enterocytes	1.08 -0.45,+0.82	12.48 -3.22,+4.39
	Dark red	Lamina propria	1.29 -0.58,+0.70	19.25 -5.06,+4.60
	Light blue	Colon epithelial cells	1.43 -0.58,+0.82	26.03 -5.15,+7.05
	Teal	Colon epithelial cells, epithelium in the vicinity of goblet cells	1.10 -0.41,+0.56	31.24 -8.11,+9.46
	Yellow	Mucus layer in lumen, interfaces	1.08 -0.30,+0.41	61.16 -14.23,+32.53
	Orange	Mucus layer in the lumen, interfaces,	1.04 -0.33,+0.47	42.41 -10.87,+13.44

Lamina propria

There appears to be an increase of pixel of the dark red class below the enterocytes. A small amount of pixels in the lamina muscularis was also assigned to the dark red cluster, which could indicate connective tissue surrounding vessels. Dark red regions can also be found within mucosal folds. These observations indicate that the dark red class is connected to the lamina propria.

Epithelium

The most prominent class in epithelium is light blue. However, a considerable amount of pixels are assigned to teal class. The location of teal pixels appears to correlate with the location of goblet cells. This could indicate an influence of scattering interferences to spectra in the teal labelled regions. Also, colour distribution might resemble the location of crypt lumina and connective tissue. Surface epithelium is largely composed of light red and dark red clusters, possibly caused by higher concentration of enterocytes.

Further findings

The yellow and orange pixel classes appear to be located at intersections of the epithelial layer to the lumen. Also, some regions of the lamina propria and mucus inside the lumen are labelled yellow and orange respectively. Contributions from scattering are enhanced by refractive index mismatching, which occurs at these locations. Refractive index mismatching is also likely in the central lumen of crypts, possibly affecting spectra of surrounding pixels, which are mostly assigned to green and teal.

In order to avoid strong over-segmentation before training of the classifier, the number of clusters was chosen to be ten. By doing so, a link between most pixel classes to tissue features was easily established. However, a larger amount of classes may be beneficial to limit the effect of scattering interferences on the analysis. The appearance of the light red (lamina muscularis) class in paraffin background could be reduced, as well as the amount of yellow and orange pixels (interferences) in the central lumen. A multi-staged cluster analysis might be

used to get more insight, without introducing a confusing amount of colors to the final representation.

Next to the good qualitative agreement among the stained images and the infrared label image, further analysis reveals deviations in the detected distribution of goblet cell rich regions (Fig. 3) between the Alcian blue and PAS stained colon slice and the label image of the adjacent slice. The lack of a solid image registration prevents a more quantitative comparison between hyperspectral imaging and standard staining: We believe that these differences are mainly due to comparing non-identical thin sections, artefacts caused by microtome cutting as well as the significant difference in slice thickness (3 μm compared to 8 μm). In turn, the correlation between the label images and the visible images of the identical, unstained slices is found to be much better. In passing we would like to note that the complexity of the clustering and classification approach may compromise sensitivity. A simplified and potentially faster strategy is provided by a dual-wavelength measurement and the distribution of mucin concentration may be visualized in gray scale images such as Fig. 5 (a).

The acquisition time for a hyperspectral image of a sample was 7.5 minutes and covered the full spectral range of 1027-1087 cm^{-1} and 1167-1319 cm^{-1} at a pixel size of 3.65 x 3.65 μm^2 and a field of view of 2.8 x 3.1 mm^2 . On the one hand, this is more time consuming than a standard H&E staining. On the other hand, H&E staining requires the tissue sample to be deparaffinized, whereas the IR spectroscopy works best in paraffinized tissue. Deparaffinizing a thin section usually takes 35 minutes.

The acquisition time for QCL-based hyperspectral imaging may be even further reduced by limiting the tuning ranges. Measurements at merely two wavenumbers (1076 cm^{-1} and 1181 cm^{-1} , see Table 1) could, for example, already suffice for high contrast imaging of goblet cell rich regions in epithelium, as shown in Fig. 5 (a).

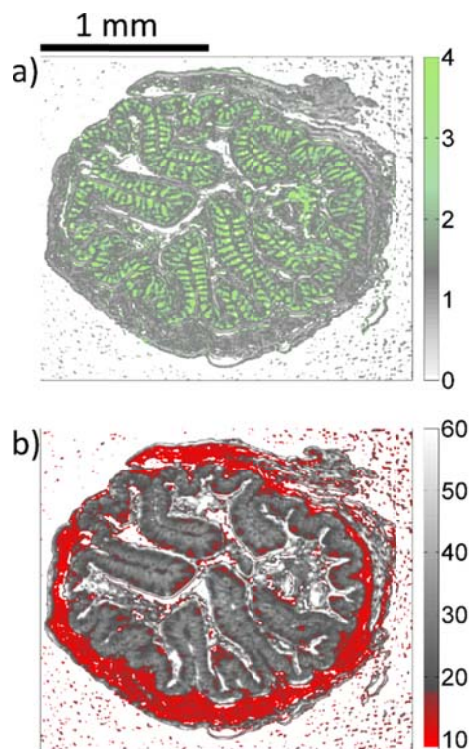


Fig. 5 Microscopic images resulting from the analysis of infrared data of the training set. (a) represents the ratio of absorbances at 1076 cm^{-1} and 1181 cm^{-1} . (b) represents the integral absorbance over the 1027 cm^{-1} - 1087 cm^{-1} spectral range (see also in Table 1).

Conclusions

We successfully demonstrated the automated detection of mucin-rich regions in mouse colon mucosa using QCL-based hyperspectral imaging and a random decision forest classifier. The total field of view of a single measurement was $3.1 \times 2.8\text{ mm}^2$. The medically relevant identification and enumeration of the mucin-containing goblet cell population may be performed within 7.5 minutes (including measurement and data analysis). Given the results presented in this manuscript the process could be further shortened down to an overall time requirement for measurement and analysis of well below 1 minute. Further experiments have to clarify to what extent the procedure could be used to augment differential diagnosis of gastrointestinal diseases and in particular the differentiation between ulcerative colitis and intestinal infections.

Acknowledgements

The authors would like to thank S. Spiegel for his technical support and E. Seelinger for sample preparation. A. Schönhals acknowledges support by the Heidelberg Graduate School of Fundamental Physics. This work was financed by the Baden-Württemberg Stiftung.

Notes and references

‡ Next to his affiliation with the Kirchhoff-Institute for Physics, W. Petrich is an employee of Roche Diagnostics GmbH, Germany.

^a Heidelberg University, Kirchhoff Institute for Physics, Im Neuenheimer Feld 227, Heidelberg, 69120 Germany

^b Heidelberg University, Medical Faculty Mannheim, Medical Research Center, Theodor-Kutzer-Ufer 1-3, Mannheim, 68167 Germany

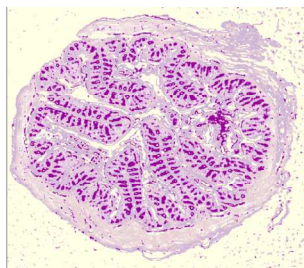
- 1 R. J. Xavier and D. K. Podolsky; „Unravelling the pathogenesis of inflammatory bowel disease”, *Nature*, 2007, 448, 427-434
- 2 D. K. Podolsky; „Inflammatory bowel disease”, *N. Engl. J. Med.*, 2002, 347, 417-429
- 3 M. Gersemann, S. Becker, I. Kübler, M. Koslowski, G. Wang, K.R. Herrlinger, J. Griger, P. Fritz, K. Fellermann, M. Schwab, J. Wehkamp and E.F. Stange; „Differences in goblet cell differentiation between Crohn's disease and ulcerative colitis.”, *J. Diff.*, 2009, 77, 84-94
- 4 D. Jenkins, M. Balsitis, S. Gallivan, M. F. Dixon, H. M. Gilmour, N. A. Shepherd, A. Theodossi and G. T. Williams; „Guidelines for the initial biopsy diagnosis of suspected chronic idiopathic inflammatory bowel disease”, *J. Clin. Pathol.*, 1997, 50, 93-105
- 5 Y. S. Kim and S. B. Ho; „Intestinal Goblet Cells and Mucins in Health and Disease: Recent Insights and Progress”, *Curr. Gastroenterol.*, 2010, Rep 12, 319-330
- 6 M. Classen, G. N. J. Tytgat and C. J. Lightdale; „Gastroenterological Endoscopy”, Thieme, Stuttgart, Germany (2010), ISBN (Americas): 9783131258526, 607-608
- 7 J. Faist, F. Capasso, D. L. Sivco, C. Sirtori, A. L. Hutchinson and A. Y. Cho; „Quantum Cascade Laser”, *Science*, 1994, 264, 553-556
- 8 M. C. Phillips and B. E. Bernacki; „Hyperspectral microscopy of explosives particles using an external cavity quantum cascade laser”, *Opt. Eng.*, 2013, 52, 061302
- 9 M. R. Kole, R. K. Reddy, M. V. Schulmerich, M. K. Gelber and R. Bhargava; „Discrete frequency infrared microspectroscopy and imaging with a tunable quantum cascade laser”, *Anal. Chem.*, 2012, 84, 10366-10372
- 10 N. Kröger, A. Egl, M. Engel, N. Gretz, K. Haase, I. Herpich, S. Neudecker, A. Pucci, A. Schönhals and W. Petrich; „Rapid hyperspectral imaging in the mid-infrared”, *Proc. SPIE*, 2014, 8939, 89390 Z-7
- 11 N. Kröger, A. Egl, M. Engel, N. Gretz, K. Haase, I. Herpich, B. Kränzlin, S. Neudecker, A. Pucci, A. Schönhals, J. Vogt and W. Petrich; „Quantum cascade laser-based hyperspectral imaging of biological tissue”, *J. Biomed. Opt.*, 2014, 19, 111607
- 12 P. Bassan, M. J. Weida, J. Rowlette and P. Gardner; „Large scale infrared imaging of tissue micro arrays (TMAs) using a tunable Quantum Cascade Laser (QCL) based microscope”, *Analyst*, 2014, 139, 3856
- 13 C. Vrancic, N. Kröger, N. Gretz, S. Neudecker, A. Pucci and W. Petrich; „A Quantitative Look Inside the Body: Minimally Invasive Infrared Analysis in Vivo”, *Anal. Chem.*, 2014, (in press, published online Oct 22nd, 2014), doi: 10.1021/ac5028808
- 14 A. Travo, O. Piot, R. Wlthuis, C. Gobinet, M. Manfait, J. Bara, M.-E. Forgue-Lafitte and P. Jeannesson, „IR spectral imaging of secreted mucus: a promising new tool for histopathological recognition of human colonic adenocarcinomas”, *Histopathology*, 2010, 56, 921-931
- 15 M. A. Cohenford, S. J. Lim, C. Brown, M. A. Chaudhry, S. Sigdel, E. Beckelhimer, B. Rigas; „FT-IR Microspectroscopy of Mouse Colon Tissues: Insight into the Chemistry of Carcinogenesis and Diagnostic Potential”, *Am. J. Pathol.*, 2012, 181, 1961-1968
- 16 W. Petrich; „From study design to data analysis”, in: P. Lasch, J. Kneipp (Eds.) “Biomedical Vibrational Spectroscopy”, Wiley & Sons, Hoboken, New Jersey, USA (2008), ISBN 978-0-470-22945-3, 315-332
- 17 P. Lasch and W. Petrich; „Data Acquisition and Analysis in Biomedical Vibrational Spectroscopy”, In: D. Moss (Ed.), Biomedical Applications of Synchrotron Infrared Microspectroscopy: A Practical Approach (2010), RSC Analytical Spectroscopy Series v. 11, Royal Society of Chemistry, Cambridge, UK, 192-225
- 18 P. Lasch, W. Haensch, D. Naumann and M. Diem; „Imaging of colorectal adenocarcinoma using FT-IR microspectroscopy and cluster analysis”, *Biochim. Biophys. Acta*, 2004, 1688, 176-186
- 19 D. M. Mayerich, M. Walsh, A. Kadjacsy-Balla, S. Mittal and R. Bhargava; „Breast histopathology using random decision forests-based classification of infrared spectroscopic imaging data”, *Proc. SPIE*, 2014, 9041, 904107-1.

Visible



stained

Mid-Infrared



unstained

Mucin density is rapidly visualized in unstained, paraffin-embedded mouse colon tissue by means of mid-infrared spectroscopy using quantum cascade lasers.

1
2
3
4
5
6
7
8
9
10
11
12
13
14
15
16
17
18
19
20
21
22
23
24
25
26
27
28
29
30
31
32
33
34
35
36
37
38
39
40
41
42
43
44
45
46
47
48
49
50
51
52
53
54
55
56
57
58
59
60